ARTICLE

Tuning Non-Radiative Decay Channels via Symmetric/Asymmetric Substituent Effects on Phenazine Derivative and Their Phototherapy Switch Between Dynamic and Thermal Process

Received 00th January 20xx,
Accepted 00th January 20xx

DOI: 10.1039/x0xx00000x

Yuxuan Li,[a] Keke Ding,[b] Haozhong Wu,[a] Qing Wan,[c] Yao Ma,[a] Yuhua Huang,[b] Zhiming Wang*[a], Weijie Zhang*[b], Jianquan Hou*[b], Ben Zhong Tang*[a]

Recently, research based on non-radiative decay process leading to photodynamic therapy or photothermal therapy has become an attractive hotspot. Of particular importance is to further achieve better performance in photosensitive dyes design. Herein, two comparable emitters (DEPZ-S, DEPZ-A) with same electronic donor-acceptor segment were prepared, but their different symmetrical pattern caused different reactive oxygen species (ROS) generation capacity and photothermal conversion capacity, respectively, which implying their non-radiative decay channels could be switched between intersystem crossing (ISC) and thermal deactivation. Theoretical simulation exhibited coincident results, and their differentiated excited-state energy levels distribution decided the non-radiative decay channels change: DEPZ-S with high intramolecular symmetry exhibited larger spin-orbit coupling (SOC) matrix and smaller energy splitting (ΔE_{ST}) between singlet and triplet states easily leading to facilitate ISC process, but asymmetric DEPZ-A with narrow band gap (ΔE_{S0S1}) and big reorganization energy reduced the potential barrier of thermal deactivation and increased its occurrence probability. After encapsulating two dyes with hydrophilic polymer matrix for improving intake efficiency, both of them displayed good phototherapy treatment effect on bladder cancer cells through dynamic or thermal process when light illuminated. This work provides a new strategy of tuning non-radiative decay channels via symmetric/asymmetric substituent effects to realize precise phototherapy.

Introduction

Organic electronic conjugated materials have been obtaining increasing research interest in the fields of new energy resources,[1-3] catalyst,[4-5] optical display,[6-10] life science[11-15] and *et al*. Their typical feature is that light-generated excitons (singlet state) dissipated energy through three decay channels of fluorescence-dominated radiative transition, and non-radiative processes of thermal deactivation and intersystem crossing (ISC) according to the Jablonski principle.[16] Recently, research attention has been paid to such non-radiative processes because of their outstanding performances, such as utilizing ISC process to generate triplet excitons with functions of catalysis or carry on photodynamic therapy (PDT) based on reactive oxygen species (ROS),[17-20] as well as exploiting thermal deactivation process to produce thermal energy for photothermal treatment (PTT),[21-22] and sea water desalination.[23] Generally, the development of phototherapy largely depends on two types of non-radiative decay processes: Intersystem crossing and Thermal deactivation.

How to switch the channels between irradiative decay and non-radiative decay (intersystem crossing and thermal deactivation) has received much attention. At present, it is widely recognized that molecular structure design is the main way to modulate the three dissipation channels at molecular level.[24] The distorted D-A structure is usually designed to enable much longer-wavelength absorption and emission, meanwhile hinders the fluorescent radiation path, so as to turn on the non-radiative decay process and developed PDT/PTT.[17] Molecules with aggregation induced emission property have multiple vibrational or rotational substituents, thus they could effectively suppress the non-radiative pathway and obtain excellent fluorescence imaging effect in aggregation.[25] Beyond that, our group found that the donors/acceptors odd-even numbers brought different effects for fluorescence quantum efficiency and ISC efficiency of photosensitizers.[26] In our view, this regulation at the molecular level might originate from the substituent effect. However, the way to switch the two non-radiative decay channels of ISC and thermal deactivation in different molecular structures was rarely discussed.

As an alkyl substituted phenazine derivative, DEPZ inherited powerful electron donor capability as Hua's group described. [27-

[a] State Key Laboratory of Luminescent Materials and Devices, Guangdong Provincial Key Laboratory of Luminescence from Molecular Aggregates, Center for Aggregation-Induced Emission, Guangzhou International Campus, South China University of Technology (SCUT), Guangzhou 510640, China. Department of Chemistry, The Chinese University of Hong Kong (CUHK), Shenzhen, Guangdong 518172, China, E-mail: wangzhiming@scut.edu.cn; tangbenz@cuhk.edu.cn.

[b] Department of Urology, The First Affiliated Hospital of Soochow University, NO. 188 Shizi Road, Suzhou 215006, China, Department of Urology, Medical Center of Soochow University, Suzhou Dushu Lake Hospital Suzhou 215000, China, E-mail: wj539@163.com; houjianquan@suda.edu.cn.

[c] School of Materials Science and Engineering, Nanchang Hangkong University, Nanchang 330063, China.

Electronic Supplementary Information (ESI) available: [details of any supplementary information available should be included here]. See DOI: 10.1039/x0xx00000x

[33] Herein, we introduced malononitrile into DEPZ to construct two comparable photosensitizers with different symmetry D-A structure, i.e. symmetric DEPZ-S and asymmetric DEPZ-A **(Figure 1)**. The separation of highest occupied molecular orbitals (HOMOs) and lowest unoccupied molecular orbitals (LUMOs) was inferred that both of them occurred strong intramolecular charge transfer (ICT) in the excited state, thus the widened absorption range and the red-shifted emission spectra were obtained compared to DEPZ. After the verification of experiment and theoretical calculation, we discovered symmetric DEPZ-S possessed great free radical ROS generation efficiency because of its smaller ΔE_{ST} and larger SOC matrix, while asymmetric DEPZ-A showed better photothermal conversion effect due to the smaller energy gap of S_0 with S_1 and bigger reorganization energy. Thanks to their desirable free radical ROS generation or photothermal conversion efficiency, DEPZ-S and DEPZ-A both had significant photo-therapeutic effect to bladder cancer cells in the processes of PDT and PTT.

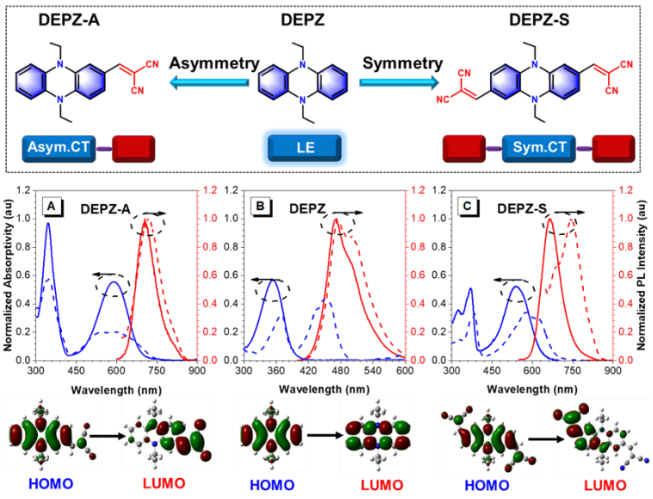

Fig. 1 Chemical structures and electron distribution of HOMOs and LUMOs of DEPZ, DEPZ-S, DEPZ-A; Absorption and emissive spectra of DEPZ-A (A), DEPZ-S(C) in THF (solid lines) and in nanoparticles (dotted lines): Concentration: 37 μM. Absorption and emissive spectra of DEPZ (B) in THF (solid lines) and THF/H_2O mixture (dotted lines): Concentration: 10 μM, V_{THF}/V_{H2O} = 1:9. Calculated method:

Results and Discussion

Synthetic route

The synthetic route was provided in Fig. S1. 5,10-dihydrophenazine was obtained from commercial phenazine via the reduction reaction using $Na_2S_2O_4$ as reductant. Thus obtained 5,10-dihydrophenazine was further reacted with bromic ether to prepare DEPZ under the alkaline environment. Next, DEPZ further participated in Friedel-Crafts acylation to obtain DEPZ-CHO and DEPZ-2CHO, respectively. Finally, malononitrile reacted with DEPZ-CHO and DEPZ-2CHO to synthesize final products (DEPZ-S and DEPZ-A) based on the Knoevenagel Condensation reaction. Their chemical structures were fully characterized by ^{1}H NMR, ^{13}C NMR and high-resolution mass spectra (Fig. S2-12).

Photoluminescence property

Photophysical properties of three emitters were firstly characterized in detail. As shown in Fig. 1, DEPZ as building block showed absorption and emission peaks at 354 nm and 471 nm in THF solution. After fabricating symmetry and asymmetry D-A fluorophores of DEPZ-S and DEPZ-A, the new absorption peaks with lower energy at 540 nm and 589 nm could be observed in such two emitters, and the photoluminescent peaks also red shifted to 665 nm and 705 nm respectively compared to DEPZ, ascribed to the intramolecular charge transfer phenomenon according to previous reports.[33] Based on the PBE0/6-31G(d, p) level, the electron distribution of HOMOs and LUMOs were calculated based on their optimized ground-state geometry to further demonstrate the transition form in the gas phase. The electrons of HOMO and LUMO in DEPZ both concentrated on the phenazine block, and displayed typical local excited (LE) feature. In contrast, DEPZ-S and DEPZ-A showed significant electrons transition from phenazine (HOMO) to malononitrile (LUMO) with ICT feature, which was in accordance with our design. To verify their ICT property, the solvation effect of absorption and emission spectra in various solvents with different polarity were collected (Fig. S13). The ground-state optical property reflected by absorption spectra suggested that they were insensitivity to environmental polarity due to the slight change of maximal absorption peaks (Fig. S13A, D, G). However, the excited-state properties of DEPZ-S and DEPZ-A were special sensitivity for solvent polarity according to the emission spectra (Fig. S13E, H). With the enhancement of solvent polarity, maximal emission peaks red shifted from deep red to near-infrared red (NIR) region, suggesting the emergence of their CT-dominated fluorescence.[34] However, the maximal emission peak of DEPZ was insensitive to polarity, which was well in accordance with the theoretical simulation, implying the presence of the LE-dominated fluorescence. The calculated transition dipoles of three emitters directly reflected electron transition form (Fig. S13C, F, I). The dipole (3.18 Debay) in DEPZ was largely smaller than DEPZ-S (12.99 Debay) and DEPZ-A (13.47 Debay), confirming strongly ICT feature in such two D-A type fluorophores. And clear photophysical data were listed in Table S1-3. DEPZ had weak fluorescence with PLQY of 5.1% in THF solution (Table 1), once aggregated, the PLQY of 29.4% suggested typical aggregation-enhanced emission (AEE) nature,[27] even though DEPZ had higher fluorescence efficiency in the solid state. 70.6% of

Table 1. Experimental Photophysical data for the PSs.

Compounds	λ_{abs}[a] [nm]		λ_{em}[b] [nm]		Φ_F[c] [%]	
	Soln	NPs	Soln	NPs	Soln	NPs
DEPZ	354	450	471	475[d]	5.1	29.4[d]
DEPZ-S	540	620	665	744	8.6	1.3
DEPZ-A	589	589	705	718	1.6	0.4

[a]Maximum absorption wavelength; [b]Maximum emission wavelength, [c]Absolute fluorescence quantum efficiency; [d]Aggregation state: in film, the chemical properties of DEPZ nanoparticles are unstable. Soln: in THF solution, concentration: 10 μM; NPs: nanoparticles dispersed in PBS, concentration: 37 μM.

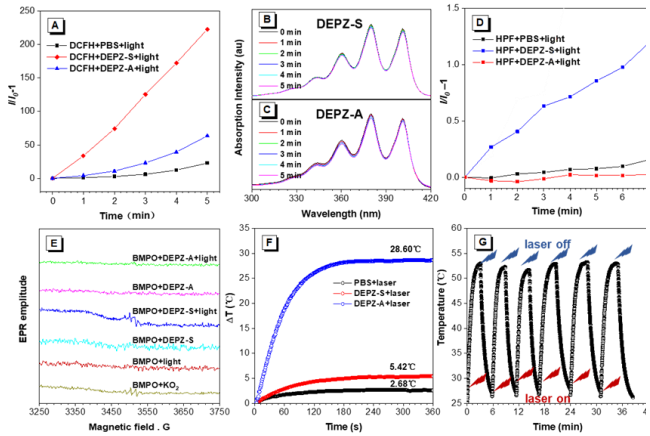

Fig. 2 (A) PL intensity change spectra of DCFH (5 μM) in the absence of PBS, DEPZ-S (10 μM) and DEPZ-A (10 μM) under the white light illumination (30 mW/cm^2). Mixture solvent DMSO/PBS (v/v = 1:9); Time-dependent absorption spectra for ABDA (0.1 mM) with (B) DEPZ-S (10 μM), (C) DEPZ-A (10 μM) in DMSO/PBS (v/v = 1:9); (D) Time-dependent changes of PL intensity (I/I_0-1) for HPF (5 μM) with PBS, DEPZ-S (10 μM), DEPZ-A (10 μM) in DMSO/PBS (v/v = 1:9). White light: 30 mW/cm^2; (E) The EPR signal of BMPO for free radical ROS characterization, concentration: BMPO (25 mM), KO^2 (10 mM), DEPZ-S (1 mM), DEPZ-A (1 mM). White light: 100 mW/cm^2; (F) Photothermal effect of PBS, DEPZ-S NPs and DEPZ-A NPs under 660 nm laser (0.5 W/cm^2) for 6 min, concentration: 37 μM; (G) Photostability test of DEPZ-A NPs: photothermal conversion curves under 660 nm laser (0.5 W/cm^2) during six laser on/off cycles.

excitons dissipated energy by non-radiative decay and indicated that DEPZ had great potential to expand the non-fluorescence process. As expected, the PLQYs of DEPZ-S and DEPZ-A in aggregation were only state 1.3% and 0.4% respectively, which not only lower than PLQYs of DEPZ (29.4%), but also lower than their corresponding in THF solution (8.6% and 1.6%). They illustrated the successful construction of charge transfer state (CT state) accelerates the non-radiative process in aggregation state.

Non-radiative decay pathways

Although two DEPZ-based emitters dissipated the excited singlet energy through non-radiative process at aggregation, which way did they choose to achieve this process? 2,7-dichlorodihydrofluorescein (DCFH), an indicator probe of ROS, could detect any types ROS production by triplet exciton energy transfer or charge transfer, and usually is applied to monitor the activity of ISC channel by the total amount of ROS. As shown in Fig. 2A, the control group of DCFH exhibited slight fluorescence enhancement after light irradiation. When DEPZ-A was added into the DCFH solution and irradiated with white light, the fluorescent intensity was improved by 60 times, suggesting the effective production of ROS after light triggering. For DEPZ-S fluorophore, in contrast, the fluorescent intensity was enhanced by nearly 220 times at the same condition. The higher intensity than DEPZ-A implied more efficient ISC process occurred in DEPZ-S.

And then, the detail ROS types of DEPZ-S and DEPZ-A were discussed detailedly. As we know, the typical ROS types could be generally distinguished as singlet oxygen and radical species, and the latter one included hydroxyl radical (OH·), superoxide anion radical (O_2^{-}·) and peroxide (O_2^{2-}).[35] Therefore, series of signal probes were employed sequentially, including 9,10-anthracenediyl-bis(methylene) dimalonic acid (ABDA) for singlet oxygen, dihydrorhodamine 123 (DHR123) and vitamin C for radical ROS compound probe reagent, hydroxyphenyl fluorescein (HPF) for hydroxyl radical, and 5-*tert*-butoxycarbonyl-5-methyl-1-pyrroline-*N*-oxide (BMPO) for radical scavenger. Interestingly, the absorption intensity of ABDA probe kept unchanged after light irradiating, implying there was no singlet oxygen ($^1O_2$) production of DEPZ-S and DEPZ-A (Fig. 2B, C). Thus, DHR 123 reagent was immediately mixed with DEPZ-based PSs, and its fluorescent intensities were improved under light irradiation (Fig. S14). After adding Vitamin C to reduce free radicals, the fluorescent intensities were quickly decreased and recovered to the initial level (before the light irradiation), which confirmed the generation of radical ROS in DEPZ-S and DEPZ-A.[20]

As shown in Fig. 2D, DEPZ-S showed a little bit responsiveness in HPF solution, but the fluorescent intensity in DEPZ-A occurred little change within a certain light irradiation time, indicating only small amount of hydroxyl radical generated in DEPZ-S. After EPR measurement employing BMPO as a radical scavenger in Fig. 2E, there was obvious free radicals signal in the sample of DEPZ-S, whose position and shape were consistent with them of the signal produced by potassium superoxide after light irradiation with suitable power density and time, [36] suggesting the component of ROS generation in DEPZ-S mainly came from O_2^{-}·. However, EPR signal was very weak in DEPZ-A, which was matched to its low quantum yield of ROS generation. In summary, ROS generated from DEPZ-S were made up of a little OH· and many O_2^{-}·, but a few ROS by the production of DEPZ-A was O_2^{-}·. Therefore, due to the better free radicals ROS efficiency of DEPZ-S, we could realize that more efficient ISC process happened in DEPZ-S.

As another non-radiative channel, thermal deactivation could translate the excited energy into thermal energy. As shown in Fig. 2F, the temperature of blank group (pure PBS solution) enhanced slightly after irradiating with 660 nm laser. DEPZ-S showed weak photothermal performance because its temperature was raised by 5.42 °C. However, DEPZ-A achieved a significant increasement of 28.60 °C in temperature, suggesting highly efficient photothermal performance. After calculation, DEPZ-S possessed lower photothermal conversion efficiency of 3.05% compared with DEPZ-A (36.27%), demonstrating that non-radiative thermal deactivation channel was dominant to dissipate the excited energy for DEPZ-A (Fig. S15). The conditions of DEPZ-A nanoparticles (NPs) concentration and light powder density were further optimized (Fig. S16), and the highest temperature could arrive to 69.7 °C after optimizing conditions, when the environmental temperature was higher than 42 °C, abnormal metabolism occurred in cancer cells,[37] DEPZ-A nanoparticles could predictably kill cancer cells by heat. Furthermore, DEPZ-A NPs had better stability and the good photothermal conversion performance could be maintained after cyclic temperature “up-down” for six times (Fig. 2G).

Based on the above data results, the energy dissipation channels of two DEPZ-based PSs thus became clear, the singlet energy of DEPZ-S preferred to converse into triplet excited state to produce ROS through ISC process, while DEPZ-A suffered from fast thermal deactivation rate to obtain higher photothermal conversion efficiency.

Theoretical calculation

Theoretical simulations of energy levels, SOC matrixs and reorganization energies were operated to discuss reasons of different non-radiative channel switch between ISC and thermal deactivation. According to previous reports, small ΔE_{ST} and large SOC matrix were two key factors of achieving a fast ISC process. As shown in Fig. 3A-C, DEPZ block had larger energy splitting (ΔE_{S1T1} = 0.58 eV) between S_1 and T_1, but DEPZ-S enjoyed reduced ΔE_{S1T2} of 0.49 eV, which was also smaller than DEPZ-A (0.66 eV). In addition, the SOC matrix of DEPZ-S (0.15 cm^{-1}) was larger than DEPZ-A (0.10 cm^{-1}). These results supported the conclusion that non-radiative ISC in DEPZ-S was more efficient than that in DEPZ-A, inducing the higher ROS efficiency.

Additionally, the small energy gap between S_0 with S_1 (ΔE_{S0S1}), and large reorganization energies promoted the non-radiative thermal deactivation process according to the law of energy gap.[38] From the energy level diagram (Fig. 3A-C), DEPZ-A and DEPZ-S all showed narrower energy gap ΔE_{S0S1} (2.4 eV and 2.17 eV) compared to DEPZ (2.81 eV), which was consistent with the experimental trend because of the longer emission wavelength of DEPZ-S, DEPZ-A than DEPZ (Table1). DEPZ-S had smaller energy gap, which was conducive to the opening of thermal deactivation channel. The reorganization energies and Huang-Rhys factors in the gas phase were discussed. Reorganization energy distribution in each frequency band shown in Fig. (3D-F), and the total reorganization energy was calculated by the sum of products of Huang-Rhys and frequencies (Fig. 3G-I). The contribution of the reorganization energies in the low frequency region (LF: less than 200 cm^{-1}) came from the motion of flexible rotation part in the molecular structure, while the energy dissipation in the high frequency region (HF: 800-1400 cm^{-1}) mainly originated from the change of the molecular bond length and bond angle. Due to a simple structure and many vibrating groups, DEPZ had a large total reorganization energy (317.9 meV), of which the LF region accounted for 14.6%, but the proportion of HF region was 58.3%. DEPZ-S showed more rigid structure due to the extended intramolecular electronic conjugation, whose the total reorganization energy was reduced to 173.4 meV (26.9 meV LF and 77.1 meV HF). For DEPZ-A, the reorganization energy in the HF zone reached 99.9 meV, which was more than DEPZ-S, and the total reorganization energy was 198.7 meV. From the single molecule to aggregate, the rotational motion in the LF region of the molecule would be inhibited, but the bond length and bond angle would not change much. Therefore, as aggregate, the proportion of the low-frequency region would be smaller, and its effect on the reorganization energies would be weakened.[39] Moreover, the HF area would be less affected. Whether in the gas phase or in the solid phase, the total reorganization energy of DEPZ-A would be larger than that of DEPZ-S, and the non-radiative thermal deactivation process became more effective. Thus DEPZ-A with the smallest ΔE_{S0S1} and biggest total reorganization energy achieved fastest thermal deactivation rate in theory, which also explained the reason that the photothermal conversion efficiency of DEPZ-A was much higher than that of DEPZ-S.

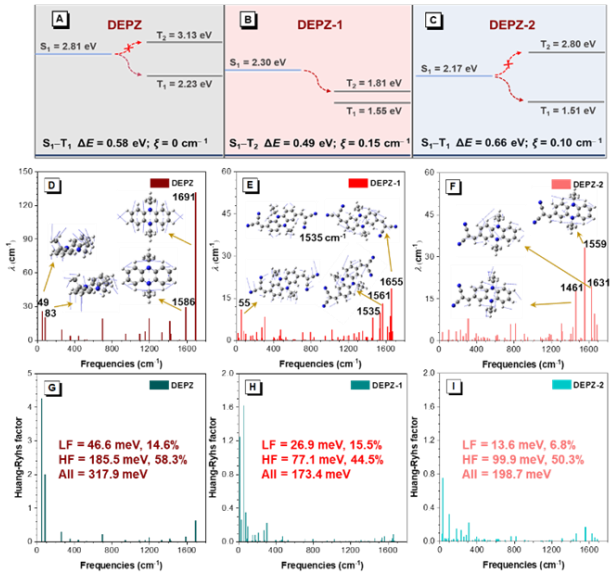

Fig. 3 Energy level diagram of excited singlet and triplet states for DEPZ (A), DEPZ-S (B), DEPZ-A (C) in gas phase. The calculated reorganization energies versus the normal mode wave numbers in gas phase of DEPZ (D), DEPZ-S (E), DEPZ-A (F) at 298 K. Calculated Huang-Rhys factors in gas phase of DEPZ (G), DEPZ-S (H), DEPZ-A (I) at 298 K, insert: values of reorganization energies in different frequency regions.

Phototherapy

Aiming at improving biocompatibility and the uptake of bladder cancer cells (MB49), DSPE-PEG_{2000}-Mal and Tat peptide were used to encapsulate the DEPZ-S to afford polymeric nanoparticles (DEPZ-S-TAT NPs) based on the nanoprecipitation method, and PDT perfomance was investigated. DEPZ-A was wrapped in DSPE-PEG_{2000}-Mal to form DEPZ-A NPs which enhanced the dispersion and water solubility to achieve PTT in cell microenvironment. (Fig. 4A).

A series of intracellular experiments were performed to conduct PDT with DEPZ-S-TAT NPs. In the first instance, ROS generated in cells was detected by DCFH-DA. According to Fig. S17, after incubating cells with DCFH-DA probe and DEPZ-S-TAT NPs without light irradiation, no fluorescent signal was discovered in cells. However, it was obvious that fluorescence could be observed after light irradiation, which demonstrated DEPZ-S-TAT NPs had entered and generated efficient ROS in the cells. DEPZ-S-TAT NPs possessed better biocompatibility and negligible toxicity as evidenced with no significant cells death although the incubated concentration arrived to 64 μM in the dark environment. After irradiating with white light, the cellular viability reduced to nearly 20%, demonstrated outstanding PDT effect (Fig. 4B). Live/death co-staining was further used to demonstrate intuitively the PDT effect of DEPZ-S-TAT NPs (Fig. 4D). After cells incubating with calcein-AM and propidium iodide (PI), the green fluorescence from calcein-AM in cells suggested they were alive, but red fluorescence from PI dye suggested that the cells were dead. There was no red fluorescence could be discovered after cells

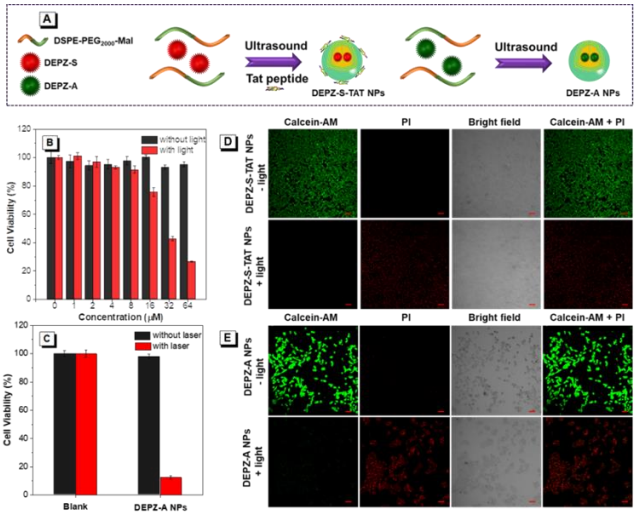

Fig. 4 (A) The preparation scheme of DEPZ-S-TAT NPs and DEPZ-A NPs. (B) Cell viability of MB49 cells stained with different concentration of DEPZ-S-TAT NPs in the absence or presence of light irradiation (50 mW/cm^2, 20 min, n=6, mean ±SD). (C) Cell viability of MB49 cells stained with PBS, DEPZ-A NPs (37 μM) in the absence or presence of 660 nm laser irradiation (0.3 W/cm^2, n=6, mean ±SD). Live/dead cell costaining of MB49 cells treated with diverse treatments assessed by Calcein-AM (green fluorescence) and PI (red fluorescence) as fluorescence probes with DEPZ-S-TAT NPs (D) and DEPZ-A NPs (E). Scale bar: 50 μm.

incubated with DEPZ-S-TAT NPs in dark environment, which demonstrated that NPs was safe enough to cells. After white light irradiation, strong red fluorescence appeared in the field of view, indicating that photo-induced ROS had killed MB49 cells.

PTT performance of DEPZ-A NPs was also evaluated, the cell viability exceeding 90% in the dark environment suggested DEPZ-A NPs were biocompatible. After treating with the 660 nm laser, the cell viability reduced largely to 10%, suggesting excellent PTT performance (Fig. 4B). From dark environment to laser irradiation, green fluorescence disappeared and red fluorescence appeared in confocal images, and live/death co-staining results also confirmed desirable PTT efficiency of DEPZ-A NPs (Fig. 4E). Therefore, DEPZ-based PSs served as suitable substrates to fabricate polymeric photo-therapeutic NPs showed promising application potential for precise phototherapy.

Conclusions

In summary, we successfully constructed symmetrical DEPZ-S and asymmetric DEPZ-A based on DEPZ (donor) and malononitrile (acceptor) by substituent effects, and achieved the tuning of two non-radiative decay channels: ISC and thermal deactivation, so as to flexibly switch the corresponding biological treatment methods. High intramolecular symmetrical DEPZ-S exhibited excellent ROS generation efficiency, because its inner features (the smaller ΔE_{ST} and larger SOC matrix) ensured highly efficient non-radiative ISC process, which further realized superb PDT performance. Meanwhile, DEPZ-A with asymmetric structure possessed narrower ΔE_{S0S1} and bigger reorganization energies, leading to more efficient thermal deactivation to boost the thermal energy production and achieve excellent PTT effect. We expected this research would provide abundant inspiration to develop diverse biotherapy technology by the change of energy release processes in the future.

Experiment Methods

Materials and instruments

All reagents and solvents were purchased through commercial channels, without secondary purification. Phenazine, sodium hydroxide, sodium hydrosulfite, phosphorus oxychloride, anhydrous magnesium sulfate, malononitrile and ammonium acetate were bought from Energy Chemical Corporation. Bromoethane was purchased from TCI Shanghai Corporation. DSPE-PEG-Mal (M_w = 2,000) was purchased from Laysan Bio Inc. (Arab, AL, U.S.A.). Phosphate-buffered saline (PBS), RPMI 1640 medium (with L-glutamine), fetal bovine serum (FBS), 0.25% Trypsin-EDTA, were obtained from Gibco™ Life Technologies. Penicillin–streptomycin (PEST) solution was purchased from Biosharp (Hefei, China). Cell viability test was measured using the Cell Counting Kit-8 (CCK8, Dojindo, Japan). 2',7'-dichlorodihydrofluorescein diacetate (DCFH-DA) were obtained from Aladdin Co., Ltd. HIV-1 Tat derivant modified with cysteine on C-terminus (RKKRRQRRRC) was customized by Genic Bio (Shanghai, China). The chemical structure of products had been confirmed by nuclear magnetic resonance, high-resolution mass spectrometry, elemental analysis and other analytical methods. ^{1}H and ^{13}C NMR spectra were recorded on a Bruker AV 400/500 spectrometer in DMSO or C_6D_6 at room temperature. High-resolution mass spectra were obtained from Agilent1290 / Bruker maXis impact. Elemental analysis results were measured by Vario EL cube. The UV-vis spectra and PL spectra were carried out by a Shimadzu UV-2600 spectrophotometer and Horiba Fluoromax-4 spectrofluorometer. The absolute fluorescence quantum efficiency was recorded on Hamamatsu absolute PL quantum yield spectrometer C11347 Quantaurus_QY. Electron paramagnetic resonance spectra were conducted on a Bruker ELEXSYS II. The Confocal laser scanning microscopy images was obtained by LSM 880 confocal laser scanning microscope.

Synthesis of 5,10-dihydrophenazine (DHPZ). Reported by other's work.[5]

Synthesis of 5,10-diethylphenazine (DEPZ). Sodium hydroxide (3.3 g, 82.4 mmol), DHPZ (5 g, 27.4 mmol) and bromoethane (6.2 ml, 82.4 mmol) were mixed and stirred at 60 °C for 6 hours in DMF (50 ml) solvent. Due to the high sensitivity of DHPZ to light and oxygen, the reaction process kept nitrogen atmosphere and avoided light. After finished, it was cooled to room temperature. The resulted liquid was poured into water, extracted with ethyl acetate in three times, and dried with anhydrous magnesium sulfate. Filtered with filter paper, the filtrate was evaporated at low pressure to obtain blue-black powder, and purified by silica gel column chromatography using petroleum ether and ethyl acetate as eluent. Finally, we got the light green crude product 3.2 g, yield 50%.^{1}H NMR (400 MHz, C_6D_6) δ 6.61 (dd, J = 3.2, 5.6 Hz, 4H), δ 6.11 (dd, J = 3.6, 6 Hz, 4H), δ 3.08 (q, J = 6.8, 14 Hz, 4H), δ 0.83(t, J = 6.8 Hz, 6H).

Synthesis of 5,10-diethylphenazine-2,7-carbaldehyde (DEPZ-2CHO). Under air atmosphere, phosphorus oxychloride (1 ml, 10.5 mmol) was added dropwise to the mixture of DMF (1 ml, 12.6 mmol) and 1,2-dichloroethane (10 ml). 5,10-diethylphenazine (1 g, 4.2 mmol) dissolved in 1,2-dichloroethane (20 ml) was slowly injected in flask and stirred 30 minutes in ice bath, and the solution turned from transparent to purple-black. Then the reaction mixture was stirred at 90 °C for 12 hours and cooled at room temperature. To neutralize the acid produced by phosphorus oxychloride, the resulted liquid was slowly dripped into the ice-water solution of sodium carbonate. The mixture was extracted with dichloromethane in three times and dried with anhydrous magnesium sulfate. After filtration and evaporation under low pressure, the red black powder was obtained, and purified by silica gel column chromatography using petroleum ether and DCM as eluent. Finally, we got the crude product 800 mg, yield 65%. ^{1}H NMR (500 MHz, DMSO) δ 9.59 (s, 2H), δ 7.22 (dd, J = 5.0, 10.0 Hz, 2H), δ 6.73(d, J = 1.5 Hz, 2H), δ 6.55(d, 2H), δ 3.58 (q, J = 7.0, 14 Hz, 4H), δ 1.15 (t, J = 6.5 Hz, 6H). HRMS ($C_{18}H_{18}N_2O_2$): m/z 317.1260 [M+, calcd 294.1368].

Synthesis of 5,10-diethylphenazine-2-carbaldehyde (DEPZ-CHO). In ice bath, phosphorus oxychloride (0.6 ml, 6.3 mmol) was added dropwise to the mixture of DMF (0.3 ml, 4.2 mmol) and 1,2-dichloroethane (10 ml). After 5,10-diethylphenazine (1 g, 4.2 mmol) had dissolved in 1,2-dichloroethane (20 ml) was slowly injected in flask and stirred 30 minutes under air atmosphere, the solution turned from transparent to purple-black. Then the reaction mixture was stirred at 90 °C for 12 hours and cooled at room temperature. To neutralize the acid produced by phosphorus oxychloride, the resulted liquid was slowly dripped into the ice-water solution of sodium carbonate. The mixture was extracted with dichloromethane in three times and dried with anhydrous magnesium sulfate. After filtration and evaporation under low pressure, the red black powder was obtained, and purified by silica gel column chromatography using petroleum ether and DCM as eluent. Finally, we got the crude product 750 mg, yield 67%. ^{1}H NMR (500 MHz, C_6D_6) δ 9.67 (s, 1H), δ 6.76 (m, 2H), δ 6.51(m, 2H), δ 5.95(dd, J = 10.0, 20.0 Hz 2H), δ 5.76(d, J = 10.0, 1H), δ 2.91 (q, J = 5.0, 15.0 Hz 2H), δ 2.84 (q, J = 5.0, 15.0 Hz 2H), δ 0.73 (t, J = 5.0Hz, 3H), δ 0.67 (t, J = 5.0Hz, 3H). HRMS ($C_{17}H_{18}N_2O$): m/z 267.1492 [M+, calcd 266.1417].

Synthesis of 2,2'-((5,10-diethyl-5,10-dihydrophenazine-2,7 diyl)bis(methanelylid- ene))dimalononitrile (DEPZ-S). The mixture of DEPZ-2CHO (400 mg, 1.0 mmol), malononitrile (excess), ammonium acetate (150 mg, 2.0 mmol) in glacial acetic acid was stirred at 120 °C for 6 hours under nitrogen atmosphere. When the raw materials had exhausted, the reaction was cooled to room temperature. The resulted mixture was poured into water and organic solids would be settled out. We purified these solids via silica gel column chromatography using petroleum ether and DCM as eluent, and got the crude product 235 mg, yield 60%.^{1}H NMR (400 MHz, DMSO) δ 8.03 (s, 2H), δ 7.30 (d, J = 8.4 Hz, 2H), δ 7.13 (d, J = 1.6 Hz, 2H), δ 6.63(s, 1H), δ 6.65 (s, 1H), δ 3.58 (q, J = 5.6, 12.4 Hz, 4H), δ 1.17 (t, J = 7.2 Hz, 6H). Found: C, 73.41; N, 21.00; H, 3.98. Calc. for $C_{24}H_{18}N_6$: C, 73.83; N, 21.52; H, 4.65%.

Synthesis of 2-((5,10-diethyl-5,10-dihydrophenazin-2-yl)methylene)malononitrile (DEPZ-A). The mixture of DEPZ-CHO (400 mg, 1.5 mmol), malononitrile (excess), ammonium acetate (231 mg, 3.0 mmol) in glacial acetic acid was stirred at room temperature for 6 hours under nitrogen atmosphere. When the raw materials had exhausted, the resulted mixture was poured into water and organic solids would be settled out. We purified these solids via silica gel column chromatography using petroleum ether and DCM as eluent, and got the crude product 320 mg, yield 68%.^{1}H NMR (400 MHz, DMSO) δ 7.87 (s, 1H), δ 7.12 (d, J = 8.4 Hz, 1H), δ 6.93 (s, 1H), δ 6.68-6.72 (m, 1H), δ 6.57-6.63 (m, 2H), δ 6.47 (t, J = 8.4, 16.8 Hz, 2H), δ 3.61 (q, J = 7.2, 14 Hz, 2H), δ 3.45 (q, J = 6.8, 14 Hz, 2H), δ 1.13 (t, J = 7.2Hz, 6H). Found: C, 77.12; N, 17.70; H, 5.40. Calc. for $C_{20}H_{18}N_4$: C, 76.41; N, 17.82; H, 5.77%.

Extracellular ROS detection.

The DCFH-DA activated by sodium hydroxide, the photosensitizer (DEPZ-S/DEPZ-A) and PBS buffer (pH=7.4) were quickly mixed uniformly, and then the fluorescence spectra were collected every minute under illumination (White light: 30 mW/cm^2). DEPZ-S or DEPZ-A from the mother liquor, were quickly added into the mixture of PBS and ABDA, and the attenuation trend of absorption spectra were recorded. The mixed solution of DHR123, sample (DEPZ-S/DEPZ-A) and PBS were added vitamin C or not, respectively. Same operations had done by mixing the PBS solution of HPF and photosensitizer (DEPZ-S, DEPZ-A), and the results have reflected on the fluorescence spectra under different illumination times (White light: 30 mW/cm^2). BMPO was added to the PBS solution containing DEPZ-S/DEPZ-A (White light: 120 mW/cm^2, 5min irradiation), superoxide anion radical ROS were detected by the EPR signal, and the control group was composed of potassium superoxide and BMPO in PBS solution.

Preparation of nanoparticles

DEPZ-S nanoparticles and DEZP-A nanoparticles were successfully prepared using the nano-deposition method,[41] but the DEPZ wasn't capable of forming stable nanoparticles originated from its chemical instability. THF solution of photosensitizer (0.5 mg/ml) and THF solution of DSPE-PEG2000-Mal (1 mg/ml) were mixed by equal volume. The mixture solution was added dropwise to ultrapure water under ultrasound, and then organic solvent would be removed from the clear emulsion by stirring and dialysis. DEPZ-A nanoparticles were obtained directly in the above steps. The DEPZ-S nanoparticles obtained above and the penetrating peptides were uniformly mixed and reacted on a shaker to form DEPZ-S-TAT NPs at 25 °C, 9 hours (C_{NPs}: C_{TAT} = 1: 3), which enhance the ability of the sample to enter the cell. The uncombined Tat peptides were removed by dialysis against PBS for two days using a 3.5 kDa molecular weight cutoff dialysis membrane.

Photothermal conversion

The PBS solution of DEPZ-S NPs/DEZP-A NPs was irradiated by 660 nm laser with the power density of 0.5 W/cm^2. The temperature detector collected data every second, and each sample was continuously irradiated for 6 minutes to detect their thermal stability via obtained temperature change curve. The temperature points of

DEPZ-S NPs/DEZP-A NPs were collected with various concentration (9.3, 18.5 and 37.0 μM) under the irradiation of 660nm laser (0.5 W/cm^{-2}) to obtain concentration-dependent photothermal curves. The power-dependent photothermal curves were also similar to the above, which used lasers with different power densities (0.3, 0.4, 0.5, 0.7 and 0.8 W cm^{-2}) to irradiate samples of the same concentration (37.0 μM). The cycle curve of heating and cooling was obtained by continuously turning on/ off the laser. The calculation of efficiency referred to published literature.[40]

Computational Methods

All theoretical data in this work were calculated based on density functional theory using Gaussian 16 package. The geometry optimizations of all compounds in the gas phase were optimized at the level of PBE0/ 6-31G (d, p), and weak intramolecular interaction was better described by using dispersion correction (DFT-D3). ΔE_{ST} and Spin-orbit coupling matrix based on the excited singlet state were carried on the M062X function and def2TZVP basis set, using Gaussian 16 package and ORCA package, respectively. Under the harmonic oscillator approximation, the reorganization energy λ_j of each normal mode was defined as its energy $h\omega_j$ multiplied by Huang-Rhys factor S_j was the displacement along each normal mode between two electronic states. The summation over all normal modes was the total reorganization energy λ.[39]

Cell culture

MB49 cells, the Mouse Bladder Carcinoma Cell Line, were kindly provided by Cell Bank/Stem Cell Bank, Chinese Academy of Sciences, and were cultured in RPMI 1640 medium supplemented with 10% FBS and 1% PEST solution at 37 °C in humidified air containing 5% CO_2.The cells were maintained exponential growth through passage before experiment.

Intracellular ROS Detection

DCFH-DA was selected for staining MB49 cells to detect intracellular ROS. MB49 cells were incubated with DEPZ-S-TAT NPs (10 μM) for 6h. After treated with DCFH-DA (10 μM) for 30min in the dark, MB49 cells were irradiated by white light (50 mW/cm^2) for 5 min before imaging by confocal laser scanning microscope (CLSM, LSM 710, Zeiss, Germany).

Cytotoxicity Assay

For cytotoxicity study, MB49 cells were seeded in 96-well plates with 3×10^3 cells per well. After incubation for 24 h, the cell culture media were replaced with DEPZ-S-TAT NPs (0 to 32 μM) or DEPZ-A NPs (0 μM，37 μM) in RPMI 1640 medium (10% FBS), respectively. For phototoxicity evaluation, after incubated in dark for 6 h, the DEPZ-S-TAT NPs treated groups were exposed to white light irradiation (50 mW/cm^2, 20 min), and the DEPZ-A NPs treated groups were exposed to 660 nm laser irradiation (0.3 W/cm^2, 10 min), followed by incubation for another 18 h. At the same time, parallel groups treated with DEPZ-S-TAT NPs or DEPZ-A NPs were incubated in dark under the same experimental environment for dark cytotoxicity evaluation. Subsequently, the cells were washed with PBS twice and incubated with fresh medium containing 10% CCK-8 for 2 h. The cell viability was calculated by absorbance of CCK-8 reaction product WST at 450 nm measured using a microplate reader (Infinite M200 Pro Tecan). The cell viability rate (VR) was calculated by the equation: $VR=OD_{sample}/OD_{control}\times100\%$.

Live/Dead cell staining

The MB49 cells were seeded in a glass-bottom confocal dish with 8×10^4 cells per dish, and incubated for 24 h. When MB49 cells reached 80% confluence, the cell culture media was replaced with DEPZ-S-TAT NPs (32 μM) or DEPZ-A NPs (37 μM) in RPMI 1640 medium (10% FBS), respectively. After 6 h incubation, DEPZ-S-TAT NPs treated cells were exposed to white light irradiation (50 mW/cm^2, 20 min), and DEPZ-A NPs treated cells were exposed to 660 nm laser irradiation (0.3 W/cm^2,10 min). At the same time, parallel groups treated with DEPZ-S-TAT NPs or DEPZ-A NPs were incubated in dark under the same experimental environment. After another 18 h incubation, the cells were stained with Calcein-AM (2 μM) and PI (8 μM) for 30 min in culture medium. After washed with PBS twice, the cells were imaged by CLSM. Conditions: PI: E_{ex} = 488 nm, E_{em} = 600 nm - 650 nm; Calcein-AM: = 488 nm, E_{em} = 500 nm - 560 nm.

Conflicts of interest

There are no conflicts to declare

Acknowledgements

National Natural Science Foundation of China (21788102, 21975077 and 82001951), National Key R&D Program of China (Intergovernmental cooperation project, 2017YFE0132200), Open Research Project of Military Logistics Support Department (BLB19J008), the Fundamental Research Funds for the Central Universities (2019ZD04), Natural Science Foundation of Guangdong Province (2020A1515011542), Natural Science Foundation of Jiangsu Province (BK20190175), Science and Technology Project for the Youth of Suzhou(KJXW2018006) and Fund of Guangdong Provincial Key Laboratory of Luminescence from Molecular Aggregates (2019B030301003).

Notes and references

1 M. Ball, Y. Zhong, B. Fowler, B. Y. Zhang, P. P. Li, G. Etkin, D. W. Paley, J. Decatur, A. K. Dalsania, H. X. Li, S. X. Xiao, F. Ng, M. L. Steigerwald, C. Nuckolls, Macrocyclization in the Design of Organic n-Type Electronic Materials, *J. Am. Chem. Soc.*, 2016, **138**, 12861.

2 C. W. Zhao, Y. T. Guo, Y. F. Zhang, N. F. Yan, S. Y. You, W. W. Li, Diketopyrrolopyrrole-based conjugated materials for non-fullerene organic solar cells, *J. Mater. Chem. A.*, 2019, **7**, 10174.

3 J. Y. Wang, R. Y. Zhu, S. J. Wang, Y. W. Li, B. Y. Jia, J. D. Zhou, P. Y. Xue, S. Seibt, Y. Z. Lin, Z. Q. Xie, W. Ma, X. W. Zhan, Enhancing photovoltaic performance via aggregation dynamics control in fused-ring electron acceptor, *Aggregate*, 2021, **2**.

4 M. A. Bryden, E. Zysman-Colman, Organic thermally activated delayed fluorescence (TADF) compounds used in photocatalysis, *Chem. Soc. Rev.*, 2021, **50**, 7587.

5 J. C. Theriot, C.-H. Lim, H. Yang, M. D. Ryan, C. B. Musgrave, G. M. Miyake, Organocatalyzed atom transfer radical polymerization driven by visible light, *Science*. 2016, **352**, 1082.

6 H. Zhang, B. Zhang, Y. W. Zhang, Z. Xu, H. Z. Wu, P. A. Yin, Z. M. Wang, Z. J. Zhao, D. G. Ma, B. Z. Tang, A Multifunctional Blue-Emitting Material Designed via Tuning Distribution of Hybridized Excited-State for High-Performance Blue and Host-Sensitized OLEDs, *Adv. Funct. Mater.*, 2020, **30**.

7 J. J. Zeng, J. J. Guo, H. Liu, Z. J. Zhao, B. Z. Tang, A Multifunctional Bipolar Luminogen with Delayed Fluorescence for High-Performance Monochromatic and Color-Stable Warm-White OLEDs, *Adv. Funct. Mater.*, 2020, **30**.

8 Q. Wan, B. Zhang, Y. Ma, Z. M. Wang, T. Zhang, B. Z. Tang, Delicate modulation of triplet energy levels for activating "hot excitons" channels in deep red AIEgens, *J. Mater. Chem. C.*, 2020, **8**, 14146.

9 J. U. Kim, I. S. Park, C. Y. Chan, M. Tanaka, Y. Tsuchiya, H. Nakanotani, C. Adachi, Nanosecond-time-scale delayed fluorescence molecule for deep-blue OLEDs with small efficiency rolloff, *Nat. Commun.*, 2020, **11**, 1765.

10 A. Salehi, X. Fu, D. H. Shin, F. So, Recent Advances in OLED Optical Design, *Adv Funct. Mater.*, 2019, **29**.

11 J. Qi, C. Chen, X. Y. Zhang, X. L. Hu, S. L. Ji, R. T. K. Kwok, J. W. Y. Lam, D. Ding, B. Z. Tang, Light-driven transformable optical agent with adaptive functions for boosting cancer surgery outcomes, *Nat. Commun.*, 2018, **9**, 1848.

12 E. Di Mauro, D. Rho, C. Santato, Biodegradation of bio-sourced and synthetic organic electronic materials towards green organic electronics, *Nat. Commun.*, 2021, **12**, 3167.

13 L. Y. Wu, Y. D. Sun, K. Sugimoto, Z. L. Luo, Y. Ishigaki, K. Y. Pu, T. Suzuki, H. Y. Chen, D. J. Ye, Engineering of Electrochromic Materials as Activatable Probes for Molecular Imaging and Photodynamic Therapy, *J. Am. Chem. Soc.*, 2018, **140**, 16340.

14 L. Y. Zhou, F. T. Lv, L. B. Liu, S. Wang, Water-Soluble Conjugated Organic Molecules as Optical and Electrochemical Materials for Interdisciplinary Biological Applications, *Acc. Chem. Res.*, 2019, **52**, 3211.

15 M. M. Kang, Z. J. Zhang, N. Song, M. Li, P. P. Sun, X. H. Chen, D. Wang, B. Z. Tang, Aggregation-enhanced theranostics: AIE sparkles in biomedical field, Aggregate., 2020, **1**, 80.

16 D. Frackowiak, The Jablonski diagram, *Journal of Photochemistry and Photobiology B: Biology*, 1988, **2**, 399.

17 W. B. Hu, T. C. He, H. Zhao, H. J. Tao, R. F. Chen, L. Jin, J. Z. Li, Q. L. Fan, W. Huang, A. Baev, P. N. Prasad, Stimuli-Responsive Reversible Switching of Intersystem Crossing in Pure Organic Material for Smart Photodynamic Therapy, *Angew. Chem. Int. Ed.*, 2019, **58**, 11105.

18 Z. J. Wang, L. Huang, Y. X. Yan, A. M. El-Zohry, A. Toffoletti, J. Z. Zhao, A. Barbon, B. Dick, O. F. Mohammed, G. Han, Elucidation of the Intersystem Crossing Mechanism in a Helical BODIPY for Low-Dose Photodynamic Therapy, *Angew. Chem. Int. Ed.*, 2020, **59**, 16114.

19 Z. M. Yang, Z. J. Zhang, Y. Q. Sun, Z. Q. Lei, D. Wang, H. C. Ma, B. Z. Tang, Incorporating spin-orbit coupling promoted functional group into an enhanced electron D-A system: A useful designing concept for fabricating efficient photosensitizer and imaging-guided photodynamic therapy, *Biomaterials*, 2021, **275**, 120934.

20 Q. Wan, R. Y. Zhang, Z. Y. Zhuang, Y. X. Li, Y. H. Huang, Z. M. Wang, W. J. Zhang, J. Q. Hou, B. Z. Tang, Molecular Engineering to Boost AIE-Active Free Radical Photogenerators and Enable High-Performance Photodynamic Therapy under Hypoxia, *Adv. Funct. Mater.*, 2020, **30**.

21 H. S. Jung, P. Verwilst, A. Sharma, J. Shin, J. L. Sessler, J. S. Kim, Organic molecule-based photothermal agents: an expanding photothermal therapy universe, *Chem. Soc. Rev.*, 2018, **47**, 2280.

22 H. Y. Wang, J. J. Chang, M. W. Shi, W. Pan, N. Li, B. Tang, A Dual-Targeted Organic Photothermal Agent for Enhanced Photothermal Therapy, *Angew. Chem. Int. Ed.*, 2019, **58**, 1057.

23 H. X. Li, H. F. Wen, J. Li, J. C. Huang, D. Wang, B. Z. Tang, Doping AIE Photothermal Molecule into All-Fiber Aerogel with Self-Pumping Water Function for Efficiency Solar Steam Generation, *ACS Appl. Mater. Inter.*, 2020, **12**, 26033.

24 G. X. Feng, G. Q. Zhang, D. Ding, Design of superior phototheranostic agents guided by Jablonski diagrams, *Chem. Soc. Rev.*, 2020, **49**, 8179.

25 J. Mei, N. L. Leung, R. T. Kwok, J. W. Lam, B. Z. Tang, Aggregation-Induced Emission: Together We Shine, *Chem. Rev.*, 2015, **115**, 11718.

26 S. J. Liu, H. K. Zhang, Y. Y. Li, J. K. Liu, L. L. Du, M. Chen, R. T. K. Kwok, J. W. Y. Lam, D. L. Phillips, B. Z. Tang, Strategies to Enhance the Photosensitization: Polymerization and the Donor-Acceptor Even-Odd Effect, *Angew. Chem. Int. Ed.*, 2018, **57**, 15189.

27 L. Yang, X. Li, Y. Qu, W. S. Qu, X. Zhang, Y. D. Hang, H. Ågren, J. L. Hua, Red turn-on fluorescent phenazine-cyanine chemodosimeters for cyanide anion in aqueous solution and its application for cell imaging, *Sensor. Actuat. B-Chem.*, 2014, **203**, 833.

28 Y. C. Yan, L. Y. Liu, C. L. Li, Z. C.Yang, T. Yi, J. L. Hua, A NIR fluorescent probe based on phenazine with a large Stokes shift for the detection and imaging of endogenous H_2O_2 in RAW 264.7 cells, *Analyst*, 2020, **145**, 4196.

29 Y. C. Yan, J. W. Chen, Z. J. Yang, X. Zhang, Z. Liu, J. L. Hua, NIR organic dyes based on phenazine-cyanine for photoacoustic imaging-guided photothermal therapy, *J. Mater. Chem. B.*, 2018, **6**, 7420.

30 X. Zhang, Y. C. Yan, Y. D. Hang, J. Wang, J. L. Hua, H. Tian, A phenazine-barbituric acid based colorimetric and ratiometric near-infrared fluorescent probe for sensitively differentiating biothiols and its application in TiO_2 sensor devices, *Chem. Commun.*, 2017, **53**, 5760.

31 Y. C. Yan, H. Fu, J. Wang, C. R. Chen, Q. Wang, Y. R. Duan, J. L. Hua, A photo-stable and reversible pH-responsive nano-agent based on the NIR phenazine dye for photoacoustic imaging-guided photothermal therapy, *Chem. Commun.*, 2019, **55**, 10940.

32 L. Yang, W. S. Qu, X. Zhang, Y. D. Hang, J. L. Hua, Constructing a FRET-based molecular chemodosimeter for cysteine over homocysteine and glutathione by naphthalimide and phenazine derivatives, *Analyst*, 2015, **140**, 182.

33 L. Yang, X. Li, J. B. Yang, Y. Qu, J. L. Hua, Colorimetric and ratiometric near-infrared fluorescent cyanide chemodosimeter based on phenazine derivatives, *ACS Appl. Mater. Inter.*, 2013, **5**, 1317.

34 Y. H. Yan, X. L. Cui, Z. Y. Li, M. M. Ding, Q. L. Che, J. Y. Miao, B. X. Zhao, Z. M. Lin, A synergetic FRET/ICT platform-based fluorescence probe for ratiometric imaging of bisulfite in lipid droplets, *Anal. Chim. Acta.*, 2020, **1137**, 47.

35 Z. Y. Zhuang, J. Dai, M. X. Yu, J. Q. Li, P. C. Shen, R. Hu, X. D. Lou, Z. J. Zhao, B. Z. Tang, Type I photosensitizers based on phosphindole oxide for photodynamic therapy: apoptosis and autophagy induced by endoplasmic reticulum stress, *Chem. Sci.*, 2020, **11**, 3405.

36 M. L. Li, T. Xiong, J. J. Du, R. S. Tian, M. Xiao, L. Y. Guo, S. Long, J. L. Fan, W. Sun, K. Shao, X. Z. Song, J. W. Foley, X. J. Peng, Superoxide Radical Photogenerator with Amplification Effect: Surmounting the Achilles' Heels of Photodynamic Oncotherapy, *J. Am. Chem. Soc.*, 2019, **141**, 2695.

37 B. Hildebrandt, P. Wust, O. Ahlers, A. Dieing, G. Sreenivasa, T. Kerner, R. Felix, H. Riess, The cellular and molecular basis of hyperthermia, *Critical Reviews in Oncology/Hematology.*, 2002, **43**, 33.

38 J. Codes, H. Heitele, M. E. Michel-Beyerle, M. Bixon, J. Jortner, Energy Gap Law for Nonradiative and Radiative

Charge Transfer in Isolated and in Solvated Supermolecules, *J. Phys. Chem.*, 1994, **98**, 1289.

39 H. Z. Wu, X. J. Song, B. Zhang, Z. M. Wang, T. Zhang, A. J. Qin, B. Z. Tang, Each phenyl group performs its own functions on luminescence: phenyl substituted effect in tetraphenylpyrazine, *Mater. Chem. Front.*, 2020, **4**, 1706.

40 R. M. Jiang, J. Dai, X. Q. Dong, Q. Wang, Z. J. Meng, J. J. Guo, Y. J. Yu, S. X. Wang, F. Xia, Z. J. Zhao, X. D. Lou, B. Z. Tang, Improving Image-Guided Surgical and Immunological Tumor Treatment Efficacy by Photothermal and Photodynamic Therapies Based on a Multifunctional NIR AIEgen, *Adv. Mater.*, 2021, **33**, e2101158.

41 G. X. Feng, J. Liu, R. R. Liu, D. Mao, N. Tomczak, B. Liu, Ultrasmall Conjugated Polymer Nanoparticles with High Specificity for Targeted Cancer Cell Imaging, *Adv. Sci.*, 2017, **4**, 1600407.